Check for updates

Structure–function mapping of host defense peptide mimics reveals strategies for antibacterial activity and eradication of mature bacterial biofilms

Xueyang Yin, ID †[a] Yufang Bi,†[a] Xiehe Wang, ID †[a] Jing Ren,[b] Jinrong Yao, ID *[a] Xin Chen, ID [a,c,d] Shengjie Ling ID *[a,c] and Zhengzhong Shao ID *[a,d]

Bacterial biofilms shield embedded cells behind extracellular polymeric substance (EPS) barriers, frustrate antibiotic penetration, and protect persisters, demanding materials that show broad antimicrobial activity coupled with efficient biofilm clearance. We establish a design framework for host defense peptide (HDP) mimics using poly(α-amino acid) copolymers with a cationic lysine backbone (degree of polymerization ≈20) and tunable hydrophobic modules—valine (Val), norvaline (Nva), phenylalanine (Phe), and *N*-ε-carbobenzoxy-lysine (CBL). Random ring-opening copolymerization of α-amino acid *N*-carboxyanhydride (NCA) (0–60% hydrophobic feed) yields amphiphilic libraries whose composition programs the secondary structure: Val biases β-sheet formation, high Nva favors α-helices, Phe promotes ordered states *via* π–π stacking, and CBL side-chain amides build stabilizing hydrogen-bond networks. Across MIC/MBC testing, *S. aureus* and *P. aeruginosa* exhibit distinct requirements: the cationic charge density is the primary determinant for penetrating EPS and clearing mature Gram-positive biofilms, whereas moderate hydrophobicity—notably Nva and CBL—optimizes activity against Gram-negative pathogens by balancing the solubility, membrane affinity, and EPS interactions. Self-assembly refines performance further; nanoscale aggregates with elevated surface potential (*e.g.*, $Lys_{60}CBL_{40}$) deepen penetration and accelerate persister eradication. Critically, the antibacterial potency against planktonic cells does not predict the antibiofilm efficacy, revealing mechanistic decoupling that necessitates independent tuning. These results deliver a quantitative structure–function map and actionable rules for engineering amphiphilic polymers that recapitulate the functional hallmarks of HDPs, enabling simultaneous planktonic killing and robust clearance of mature biofilms and offering promising candidates for multidrug-resistant, biofilm-associated infections.

Green foundation

1. This study establishes a sustainable polymerization strategy for host defense peptide mimics *via* propylene-oxide-assisted *N*-carboxyanhydride (NCA) chemistry, achieving green synthesis of biodegradable poly(α-amino acid) copolymers with tunable amphiphilicity and potent antibacterial/biofilm-clearing functions.

2. The process eliminates inert gas protection and anhydrous conditions, replaces hazardous acid scavengers with benign propylene oxide, and markedly reduces solvent use, energy input, and chemical waste; efficacy: ≥80% *S. aureus* biofilm clearance at 125–175 μg mL⁻¹, 50–80% *P. aeruginosa* biomass reduction at 200 μg mL⁻¹, MIC 3.13 μg mL⁻¹; nanoscale (+17.3 mV) aggregates deepen EPS penetration.

3. The method enables scalable, benign-by-design production of antimicrobial polymers derived from renewable amino acids. Future research will further establish it as a safer, low-waste alternative to antibiotic-based infection control while advancing sustainable healthcare and green manufacturing.

[a]*State Key Laboratory of Molecular Engineering of Polymers, Research Center of AI for Polymer Science, Department of Macromolecular Science, Fudan University, Shanghai 200433, China. E-mail: yaoyaojr@fudan.edu.cn, lingshengjie@fudan.edu.cn, zzshao@fudan.edu.cn*

[b]*School of Physical Science and Technology, ShanghaiTech University, Shanghai 201210, China*

[c]*Shanghai Stomatological Hospital & School of Stomatology, Fudan University, Shanghai 200433, China*

[d]*Laboratory of Advanced Materials, Fudan University, Shanghai 200433, China*

† These authors contributed equally to this work.

1. Introduction

Bacterial biofilms represent a major challenge for antimicrobial therapy.[1] Compared with planktonic cells, biofilm-embedded bacteria are shielded by an extracellular polymeric substance (EPS) matrix that impedes drug penetration and protects dormant persisters, rendering conventional antibiotics largely ineffective.[2] Biofilms are common in chronic wounds, implants, and device-associated infections, where antibiotic

overuse further accelerates resistance development.[3] These challenges underscore the urgent need for new antimicrobial strategies with broad-spectrum activity, high penetration, and low resistance potential.

Host defense peptide (HDP) mimics have emerged as promising materials for combating bacterial infections and biofilm-associated diseases.[4,5] However, most current efforts focus on molecular activity[5] rather than on the efficiency and sustainability of their synthesis. In recent years, the green chemistry community has emphasized quantifiable metrics—such as the E-factor,[6] process mass intensity (PMI),[7] energy consumption, and life-cycle considerations[8]—as essential criteria for evaluating chemical processes. These quantitative indicators provide a unifying framework for assessing the environmental improvement and resource efficiency. Integrating these concepts into the development of bioactive polymers enables a direct link between molecular design and sustainable manufacturing.[9]

In parallel, it has become increasingly important to evaluate the environmental impact of antimicrobial strategies themselves. Conventional antibiotics often persist in aquatic environments and contribute to the propagation of antimicrobial resistance genes,[10] whereas host defense peptides and their synthetic analogues are typically biodegradable and exhibit minimal long-term persistence.[11] From a green chemistry standpoint, HDP-based systems therefore offer the potential to reduce environmental loading and resistance risk while maintaining the therapeutic efficacy.[12]

In this context, the present study explores how structural variations in cationic copolypeptides influence both biological efficacy and process efficiency. By combining compositional tuning with analysis of material and energy use, we establish composition–structure–function relationships that are relevant not only to antibacterial performance but also to process greenness. This dual perspective bridges molecular functionality with sustainable synthesis, in line with the current direction of green chemistry research. Furthermore, by comparing the sustainability profile of peptide-based antimicrobials with conventional antibiotics on a functional basis (*i.e.*, achieving ≥90% biofilm clearance), this study also highlights how biomimetic peptide design can contribute to the broader sustainability goals of green chemistry through lower persistence, reduced dosage, and improved life-cycle performance.

2. Materials and methods

2.1 Chemicals and reagents

All reagents were used as received without further purification unless otherwise stated. The main chemicals included *N*-ε-*tert*-butyloxycarbonyl-L-lysine (Boc-L-Lys, 97%), L-norvaline (L-Nva, 99%), tetrahydrofuran (THF, 99.9%, anhydrous), methyloxirane (≥99.5%), triphosgene (99%), anhydrous magnesium sulfate (AR), ethyl acetate (distilled grade), *n*-hexane (AR), L-valine *N*-carboxyanhydride (L-Val NCA, 98%), L-phenylalanine *N*-carboxyanhydride (L-Phe NCA, 98%), *N*-ε-carbobenzoxy-lysine NCA (L-CBL NCA, 98%), lithium bis(tri-

methylsilyl)amide (LiHMDS, 97%), and trifluoroacetic acid (TFA, ≥99.5%). All solvents were supplied by commercial vendors and used directly in synthesis and polymerization procedures. General handling and analytical procedures followed established protocols.[13]

2.2 Synthesis and characterization of NCA monomers

Synthesis of Boc-L-Lys NCA. *N*-ε-*tert*-butyloxycarbonyl-L-lysine NCA (Boc-L-Lys NCA) was synthesized following a moisture-tolerant and acid-neutralizing protocol (Fig. S1). Conventional NCA synthesis often suffers from hydrolysis due to the generation of HCl, which causes rapid decomposition under humid conditions. Here, methyloxirane was used as an acid scavenger instead of α-pinene, eliminating the need for inert gas protection or strictly anhydrous conditions and significantly shortening the reaction time.[14] Boc-L-Lys (1.0 g, 4.1 mmol) was dissolved in 20 mL THF, followed by the addition of methyloxirane (2.8 mL, 40.6 mmol) under magnetic stirring. Triphosgene (620 mg, 2.1 mmol) was then added in one portion, and the sealed pressure vessel was stirred at room temperature for 3 h. The reaction was quenched by adding 10 mL of chilled deionized water (4 °C), and the product was extracted twice with ethyl acetate (2 × 20 mL). The combined organic phases were washed with saturated brine, dried over anhydrous MgSO$_4$, and evaporated under reduced pressure. The residue was recrystallized from *n*-hexane/ethyl acetate (<10 °C) to afford Boc-L-Lys NCA as white crystals (yield = 74%).

The successful synthesis of Boc-L-Lys NCA was confirmed by ^{1}H and ^{13}C NMR (Fig. S2 and S3). In the ^{1}H NMR spectrum (400 MHz, CDCl$_3$), the characteristic NCA ring proton appears at δ 6.88 (s, 1H); the α-CH of lysine at δ 4.33 (dd, J = 6.8, 4.7 Hz, 1H); a singlet at δ 3.14 (2H) corresponds to the ε-CH$_2$; multiplets at δ 2.07–1.94 and 1.91–1.77 (each 1H) and 1.63–1.45 (4H) arise from the aliphatic methylenes; and the Boc *tert*-butyl group resonates at δ 1.45 (s, 9H). The ^{13}C NMR spectrum (100 MHz, CDCl$_3$) further corroborates the structure, showing carbonyl carbons at δ 169.9 (NCA) and 152.1 (carbamate), the Boc quaternary carbon near δ 77.3, the α-carbon at δ 57.5, and aliphatic/*tert*-butyl carbons at δ 29.2, 28.4, and 21.1. These assignments are consistent with previous reports for Boc-protected lysine NCAs.[14]

Synthesis of L-Nva NCA. L-Nva NCA was prepared by triphosgene-mediated cyclization under a nitrogen atmosphere (Fig. S4). L-Nva (1.0 g, 8.5 mmol) was suspended in 30 mL anhydrous THF. Triphosgene (1.1 g, 3.7 mmol) dissolved in 10 mL THF was added dropwise under ice cooling, followed by refluxing at 50 °C for 1 h under nitrogen. After solvent removal under reduced pressure, the residue was dissolved in ethyl acetate (30 mL), washed with ice-cold deionized water (3 × 30 mL) and saturated brine, dried over MgSO$_4$, and recrystallized from *n*-hexane/ethyl acetate to give white needle-like crystals (735 mg, 60%).

The successful synthesis of L-Nva NCA was confirmed by ^{1}H NMR (Fig. S5). In the ^{1}H NMR spectrum (400 MHz, CDCl$_3$), the characteristic NCA ring proton appears at δ 6.88 (s, 1H); the α-CH resonates at δ 4.34 (dd, J = 6.9, 5.3 Hz, 1H); signals for the aliphatic methylenes are observed at δ 1.91 (ddd, J = 15.9, 9.7, 5.4

Hz, 1H), 1.86–1.71 (m, 1H), and 1.60–1.36 (m, 2H); and the terminal CH_3 appears as a triplet at δ 0.99 (t, J = 7.3 Hz, 3H).

2.3 Synthesis of random copolymers

Ring-opening copolymerization. Random copolymers P(L-Lys$_{x\%}$-co-Y$_{y\%}$)$_{20}$ were synthesized *via* LiHMDS-initiated ring-opening polymerization of NCA. Taking Lys$_{90}$Val$_{10}$ as a representative example, Boc-L-Lys NCA (50.0 mg, 0.18 mmol) and L-Val NCA (2.9 mg, 0.02 mmol) were dissolved in 2 mL THF. A 0.1 M LiHMDS solution (0.4 mL) was rapidly added under stirring at room temperature. After completion (monitored by TLC), the reaction was quenched with formic acid. The polymer solution was diluted to 5 mg mL^{-1} in DMF (containing 0.01 M LiBr) and analyzed by GPC (Agilent/Wyatt, A31-3 column). The remaining solution was poured into *n*-hexane (40 mL) to precipitate the polymer, followed by repeated redissolution/precipitation cycles in THF/*n*-hexane. The Boc-protected copolymer was isolated as a white solid (yield = 82%).

Deprotection. Boc groups were removed using TFA at 0 °C. The polymer (50 mg) was dissolved in 1 mL TFA and stirred for 2 h under ice bath conditions. Excess acid was evaporated under nitrogen, and the polymer was precipitated with diethyl ether. The dissolution–precipitation cycle was repeated three times (methanol/ether), yielding deprotected cationic copolymers, confirmed by ^{1}H NMR (Fig. S6–S9).

2.4 Evaluation of process efficiency and greenness

Quantitative indicators commonly adopted in green chemistry were employed to evaluate the process efficiency, including the E-factor (ratio of waste to product), PMI, and energy consumption per kilogram of product. PMI (process mass intensity) was defined as:

$$PMI = \frac{\sum m_{inputs}}{m_{isolated\ product}} \quad (1)$$

Unless otherwise noted, PMI refers to materials PMI (excludes solvents and water); the complete PMI (cPMI) including solvents/water is provided in the SI together with solvent-recovery assumptions.[15–17] These metrics provide a direct measure of material and energy utilization efficiency during polymer synthesis.

For comparison, a conventional α-pinene/HCl-based NCA synthesis was analyzed as a representative benchmark. The present moisture-tolerant, catalyst-free route proceeds at ambient temperature within 3 h, in contrast to 60 °C for 12 h under nitrogen protection required by the traditional process. This modification leads to an approximately twofold reduction in energy demand and a decrease of E-factor and PMI values from 51.2 to 22.5 and from 11 to 5, respectively (Table 1). Such quantitative evaluation allows comparison of the synthesis efficiency on an environmental basis consistent with current green chemistry practices.[18–23]

2.5 Antibacterial activity evaluation

The antibacterial activity of the cationic polypeptide polymers was evaluated by determining the minimum inhibitory concentration (MIC), minimum bactericidal concentration (MBC), and the killing efficiency against persister cells. MIC tests were conducted following a standard protocol described previously.[24] *S. aureus* (ATCC 6538) and *P. aeruginosa* (ATCC 9027) (obtained from the Shanghai Collection of Microorganisms) were inoculated into 10 mL LB medium and incubated at 37 °C with shaking for 12 h. The bacterial cultures were harvested by centrifugation, resuspended, and diluted with Mueller–Hinton (MH) broth to the desired concentration.

In a sterile 96-well plate, serial two-fold dilutions of the polymer solution were prepared in MH medium, and 50 μL of each dilution was mixed with an equal volume of bacterial suspension (2×10^5 CFU per mL). Wells containing only bacterial suspension and only MH broth served as the control and blank, respectively. After static incubation at 37 °C for 9 h, the optical density at 600 nm (OD$_{600}$) was measured using a multi-

Table 1 Quantitative comparison between conventional α-pinene/HCl and epoxide-neutralized NCA synthesis routes[25,26,28,31–33]

Parameter	Conventional α-pinene/HCl route	Moisture-tolerant epoxide-neutralized route (this work)	Improvement (%)
Reaction temperature/time	60 °C × 12 h (under N$_2$)	25 °C × 3 h (ambient, sealed vial)	≈80 ↓ thermal input
Catalyst/acid neutralizer	α-Pinene (10 eq.) + triphosgene	Propylene oxide (10 eq.) + triphosgene	— (eliminates hazardous acid gas)
Inert-gas requirement	Continuous N$_2$/Ar purge	Not required (sealed system)	100 ↓
Yield (%)	~60%	74%	+20 ↑
Main by-products	HCl + chlorinated residues	1-Chloro-2-propanol/2-chloro-1-propanol (acid-catalyzed ring-opening products of PO); removable during work-up	Non-corrosive/low toxicity
Energy consumption (kWh kg^{-1} product)	10	5	−50 ↓
E-factor (waste/product)	51.2	22.5	−56 ↓
Process mass intensity (PMI)	11	5	−55 ↓
Overall assessment	High energy input and corrosive by-products	Low energy input, benign by-products, higher yield	—

Conventions: PMI excludes solvents/water unless noted; cPMI (gross & net; 90% recovery for THF/EtOAc) is provided in the SI S1.

mode microplate reader (Cytation 3, BioTek). Bacterial viability was calculated using the following eqn (2).

$$\text{Bacterial viability } (\%) = \frac{OD_{600,\,sample} - OD_{600,\,blank}}{OD_{600,\,control} - OD_{600,\,blank}} \times 100\% \quad (2)$$

For MBC determination, 3.5 μL of the bacterial suspension from each MIC well was spotted onto LB agar plates and incubated at 37 °C for 12 h; the lowest polymer concentration yielding no visible colonies was recorded as the MBC. Persister cell killing assays were performed using *S. aureus* (ATCC 6538) grown to the logarithmic phase in LB medium. The cells were collected, resuspended in MH broth to 10^8 CFU per mL, and treated with ciprofloxacin (CIP, 10 × MIC) for 18 h under static conditions to induce persister formation. The persister cells were divided into two groups: one treated with CIP (10 × MIC) and the other with the poly(α-amino acid) solution (4 × MIC). At 6 h intervals, aliquots were withdrawn, plated on LB agar, and incubated overnight at 37 °C for colony counting. The number of surviving colonies was used to quantify the bactericidal efficiency of the polymers against antibiotic-tolerant persister cells.

2.6 Antibiofilm activity evaluation

The antibiofilm performance of the cationic polypeptide polymers was evaluated by assessing their ability to inhibit biofilm formation and disrupt the preformed biofilms of *S. aureus* (ATCC 6538) and *P. aeruginosa* (ATCC 9027). For inhibition assays, bacterial cells were harvested by centrifugation and resuspended in MH broth supplemented with 1% glucose to a final concentration of 2×10^6 CFU per mL. Polymer solutions were serially two-fold diluted in MH medium containing 1% glucose in tissue-culture-treated 96-well plates, with a final volume of 50 μL per well. Subsequently, 50 μL of the bacterial suspension was added to each well and mixed thoroughly, followed by static incubation at 37 °C for 24 h. Wells containing only MH broth (100 μL) served as negative controls, while those containing 50 μL MH and 50 μL bacterial suspension served as positive controls.

For disruption assays, mature *S. aureus* biofilms were established by inoculating 100 μL of a 10^5 CFU per mL bacterial suspension (prepared in MH medium) into tissue-culture-treated 96-well plates and incubating statically at 37 °C for 24 h. The supernatant was then discarded, and the wells were gently rinsed with PBS to remove planktonic cells. Diluted polymer solutions (200 μL) were carefully added to each well containing preformed biofilms, followed by incubation at 37 °C for 24 h. The viability of biofilm-embedded bacteria was quantified using an MTT assay.

For *P. aeruginosa* biofilms, bacterial cells were harvested, resuspended in SOB medium, and adjusted to 10^5 CFU per mL. A 100 μL aliquot of this suspension was transferred into tissue-culture-treated 96-well plates and incubated statically at 37 °C for 36 h to allow biofilm maturation. The supernatant was removed, and the wells were washed once with PBS to remove planktonic bacteria. Polymer solutions were serially diluted in MH medium from an initial concentration of 200 μg mL^{-1}, and 200 μL of each

dilution was added to the biofilm-containing wells. After static incubation at 37 °C for 9 h, MTT staining was performed to determine bacterial metabolic activity.

For MTT staining, the treated biofilms were rinsed gently with PBS, and 100 μL of MTT working solution (0.5 mg mL^{-1} in PBS) was added to each well. The plates were incubated at 37 °C for 4 h in the dark. After removing the supernatant, 100 μL of DMSO was added to dissolve the formazan crystals, and the absorbance at 570 nm was measured using a multimode microplate reader. Bacterial viability was calculated using eqn (3):

$$\text{Bacterial viability } (\%) = \frac{A_{570,\,sample} - A_{570,\,blank}}{A_{570,\,control} - A_{570,\,blank}} \times 100\% \quad (3)$$

Confocal laser scanning microscopy (CLSM, Nikon C2+) was employed to visualize the biofilm morphology and cell viability after polymer treatment. Prior to imaging, biofilms were stained with 25 μL SYTO 9 (3 μM) and 25 μL propidium iodide (PI, 15 μM) for 5 min. SYTO 9 was excited at ~500 nm with emission at ~530 nm and PI was excited at ~493 nm with emission at ~636 nm.

For surface morphology observation, biofilms on cell-culture coverslips were treated with the respective polymer solutions and examined using field-emission scanning electron microscopy (SEM, Gemini SEM 500, Zeiss). Following treatment, the biofilms were rinsed gently with PBS and fixed overnight at 4 °C with 4% glutaraldehyde. After fixation, samples were dehydrated through a graded ethanol series (30, 50, 70, 80, 90, 95, and 100% v/v), dried, and subjected to SEM analysis to evaluate the extent of biofilm disruption.

2.7 Cytotoxicity

NIH/3T3 cells were evaluated by CCK-8 viability analysis after 24 h exposure to polymers at 50, 100, 125, 150, 175, and 200 μg mL^{-1}; cells were seeded at 8×10^3 cells per well in DMEM + 10% FBS and the absorbance was read at 450 nm. The full protocol is provided in the SI.

2.8 Characterization

Molecular weights were determined by gel permeation chromatography (GPC) in DMF containing 0.01 M LiBr at 50 °C (flow rate 1.0 mL min^{-1}) using PolarGel-L (and, when required, PolarGel-M) columns. ^{1}H NMR spectra of polymers were acquired in D$_2$O on a Bruker AVANCE III HD spectrometer to verify composition and deprotection. Circular dichroism (CD) spectra were recorded on a Chirascan spectropolarimeter (Applied Photophysics) at 25 °C using polymer solutions (200 μg mL^{-1} in PBS, pH 7.4) in 1 mm quartz cuvettes over 195–280 nm (1 nm interval, 50 nm min^{-1} scan rate, 2 nm bandwidth); the mean residue ellipticity was calculated as $[\theta]$ (deg cm^2 dmol^{-1}) = mdeg/($l \times c$), where mdeg is the CD signal, l is the path length (mm), and c is the molar concentration (mM). Critical aggregation concentrations (CACs) were determined with 8-anilino-1-naphthalenesulfonic acid (ANS, 10 μM) as a fluorescent probe by preparing polymers at 0.03–400 μg mL^{-1}

in PBS (pH = 7.4) or PB (pH = 5.5), incubating for 1 h at room temperature in the dark, and recording emission spectra from 420–670 nm (λ_{ex} = 360 nm); CAC values were obtained from the intersection of two linear fits of fluorescence intensity *versus* log[polymer].

3.   Results and discussion

3.1   Design strategy for constructing host defense peptide mimics

Although HDP mimics display broad structural diversity, they generally share two hallmarks: cationic charge, which promotes electrostatic adsorption to anionic bacterial membranes, and amphiphilicity, which enables insertion into lipid bilayers and disruption of membrane integrity.[25] Guided by these features, we established a polymer library with varied cationic and hydrophobic modules to explore structure–function relationships.[26]

Poly(α-amino acids) were selected as the cationic framework due to their resemblance to natural HDPs and tunable side chains. Primary amines were introduced as charge carriers, as they facilitate initial membrane binding and have been reported to surpass tertiary and quaternary amines in membrane perturbation.[27]

Hydrophobicity was tuned by four representative monomers. Valine offered moderate hydrophobicity to balance solubility and insertion; norvaline increased side-chain flexibility and thus backbone conformational freedom; phenylalanine, with an aromatic ring, enhanced lipophilicity and rigidity, favoring stable membrane insertion; and CBL introduced amide groups, enabling hydrogen bonding with membrane phosphates and enhancing activity.[28]

Finally, the chain length was set at ∼20 residues, informed by previous reports that polymers shorter than this lack insertion capability, whereas longer chains suffer from reduced solubility, altered charge density, and diminished activity.[29,30] This design ensured a balance among conformational adaptability, solubility, and antibacterial performance, providing a robust platform for subsequent studies.

The process operates under mild conditions and affords Boc-L-Lys NCA as white crystals (yield = 74%). Relative to the α-pinene/HCl route, the reaction temperature and duration are markedly reduced, resulting in roughly half the energy consumption and approximately 40% lower overall waste generation. These outcomes illustrate that modifications at the process level can directly enhance the material and energy efficiency while maintaining the product yield. Our comparisons cover conventional chlorinated protocols and moisture-tolerant scavenger strategies reported in the literature,[25,26] with side-by-side conditions summarised in Table 1.

3.2   Synthesis of HDP mimics *via* NCA ring-opening polymerization

To systematically probe how the hydrophobic content affects antibacterial and antibiofilm performance, we synthesized a series of copolymers with the general formula P(Lys$_{x\%}$-*co*-Y$_{y\%}$)$_n$

(n = 20), where Y represents Val, Nva, Phe, or CBL. For clarity, they are denoted as Lys$_x$Val$_y$, Lys$_x$Nva$_y$, Lys$_x$Phe$_y$, and Lys$_x$CBL$_y$, with x and y indicating the molar ratios of Lys and the hydrophobic unit.

Cationic Boc-L-Lys NCA and four hydrophobic NCAs (L-Val, L-Nva, L-Phe, L-CBL) were synthesized and copolymerized through random NCA ring-opening, yielding amphiphilic polymers containing both cationic (Lys) and hydrophobic segments. To avoid solubility loss from excessive hydrophobicity, feed ratios were limited to 0–60%, producing representative libraries for each class (Fig. 1).[31]

^{1}H NMR confirmed that incorporated monomer ratios closely matched feed compositions, validating reproducibility, although Val-rich copolymers (≥50%) showed slightly lower incorporation due to reduced solubility in THF during polymerization. Gel permeation chromatography (GPC) revealed number-average molecular weights of 3–5 kDa (≈20 residues) and dispersities of 1.3–1.7. Lys$_x$Phe$_y$ and Lys$_x$CBL$_y$ showed narrower distributions (Đ ≈ 1.3), while Val- and Nva-rich copolymers were broader (Đ ≈ 1.4–1.7), likely reflecting β-sheet tendencies of Val or higher chain flexibility of Nva. Val incorporation >40% also led to solubility loss, limiting accurate GPC analysis, whereas Nva-containing copolymers retained partial solubility (Table 2). From a process standpoint, maintaining solution polymerisation under ambient THF conditions defines an operational window that minimises solvent load and enables solvent recovery, consistent with Green Chemistry practice.[33]

Because NCA copolymerization is statistical, short-range sequences are heterogeneous, with alternating, blocky, or mixed motifs. Importantly, this heterogeneity did not compromise the antibacterial or antibiofilm performance; rather, it recapitulated the structural diversity of natural HDPs and enriched the library for subsequent structure–activity studies.

3.3   Conformational analysis of HDP mimics as a function of composition

The secondary structures of HDP mimics in aqueous environments were investigated using far-UV circular dichroism (CD) spectroscopy in PBS, which better simulates physiological conditions. Spectra between 190–250 nm capture amide transitions and reveal conformational states: random coils show a positive band at ∼216 nm and a negative band near 197 nm; α-helices exhibit minima at 208 and 222 nm and β-sheets display a negative band near 216 nm and a positive signal around 195 nm.

In the Lys$_x$Val$_y$ series (Fig. 2a), 10–40% Val yielded spectra characteristic of random coils, consistent with electrostatic repulsion among Lys residues. At 50% Val, mixed α-helix/β-sheet features emerged, while 60% Val favored β-sheet structures with a strong 217 nm minimum. This progression agrees with the known β-sheet bias of Val, driven by steric restrictions from isopropyl side chains.[34–36] Lys$_x$Nva$_y$ (Fig. 2b) displayed similar trends at 10–50% Nva, but at 60% formed stable α-helices, indicated by $[\theta]_{222}/[\theta]_{208}$ ratio >1, suggesting interhelical stabilization.[37]

For Lys$_x$Phe$_y$ (Fig. 2c), increasing the Phe content weakened the 197 nm negative band, which became positive at 60%,
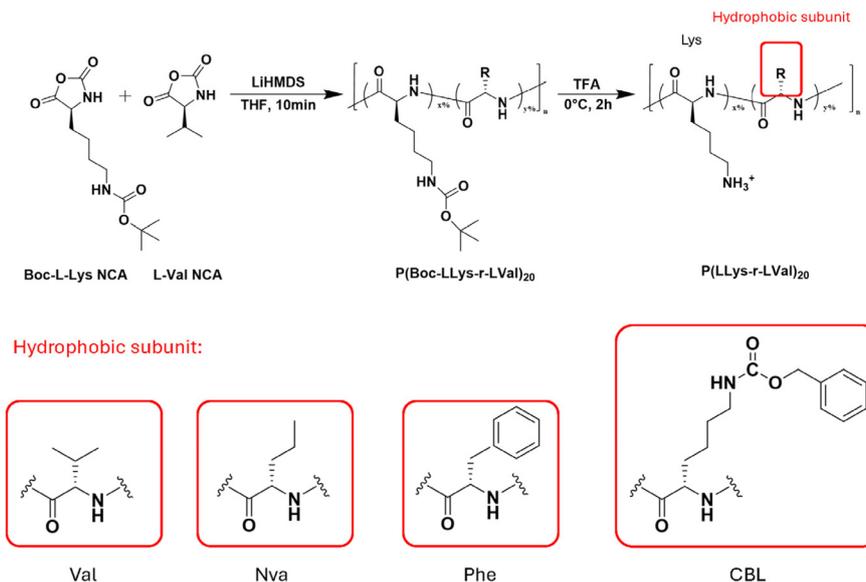
Fig. 1 Synthesis of a cationic peptide polymer by LiHMDS-initiated polymerization of α-NCA monomer.

Table 2 Physicochemical characteristics (M_n, Đ, and DP) and antimicrobial activities (MIC, MBC, and $SMIC_{80}$) of the cationic peptide polymers against *S. aureus* and *P. aeruginosa*

Series		GPC			NMR ($x\%:y\%$)	*S. aureus* 6538		*P. aeruginosa* 9027		
		M_n	Đ	DP		MIC	MBC	MIC	MBC	$SMIC_{80}$
Lys_xVal_y	$Lys_{90}Val_{10}$	5000	1.50	23	91:9	6.25	6.25	25	50	100
	$Lys_{80}Val_{20}$	4200	1.73	21	83:17	6.25	6.25	25	50	100
	$Lys_{70}Val_{30}$	4200	1.75	22	73:27	6.25	12.5	25	50	50
	$Lys_{60}Val_{40}$	4700	1.74	27	64:36	6.25	12.5	12.5	25	50
	$Lys_{50}Val_{50}$	—	—	—	56:44	12.5	200	25	100	100
	$Lys_{40}Val_{60}$	—	—	—	48:52	25	50	25	200	200
Lys_xNva_y	$Lys_{90}Nva_{10}$	5500	1.41	25	90:10	6.25	6.25	50	50	100
	$Lys_{80}Nva_{20}$	5000	1.41	25	81:19	6.25	6.25	25	50	50
	$Lys_{70}Nva_{30}$	4100	1.55	22	70:30	6.25	12.5	12.5	25	50
	$Lys_{60}Nva_{40}$	3700	1.60	21	60:40	12.5	25	3.13	25	25
	$Lys_{50}Nva_{50}$	3000	1.73	18	50:50	25	100	3.13	12.5	25
	$Lys_{40}Nva_{60}$	2800	1.76	19	43:57	25	50	6.25	25	50
Lys_xPhe_y	$Lys_{90}Phe_{10}$	4900	1.32	22	90:10	6.25	6.25	50	100	100
	$Lys_{80}Phe_{20}$	4900	1.30	23	80:20	6.25	6.25	25	50	100
	$Lys_{70}Phe_{30}$	4800	1.32	24	70:30	6.25	6.25	12.5	50	50
	$Lys_{60}Phe_{40}$	4500	1.32	23	62:38	6.25	12.5	6.25	12.5	50
	$Lys_{50}Phe_{50}$	4300	1.31	23	52:48	12.5	12.5	6.25	25	50
	$Lys_{40}Phe_{60}$	4400	1.33	25	38:62	25	50	12.5	50	100
Lys_xCBL_y	$Lys_{90}CBL_{10}$	5100	1.29	22	92:8	6.25	6.25	50	100	100
	$Lys_{80}CBL_{20}$	5100	1.30	21	80:20	6.25	6.25	25	25	50
	$Lys_{70}CBL_{30}$	5100	1.31	21	68:32	6.25	12.5	12.5	12.5	25
	$Lys_{60}CBL_{40}$	5200	1.27	21	60:40	12.5	12.5	12.5	12.5	50
	$Lys_{50}CBL_{50}$	5300	1.27	21	51:49	12.5	25	12.5	25	50
	$Lys_{40}CBL_{60}$	5500	1.28	21	48:52	25	50	25	50	100

reflecting π–π stacking that promotes ordered conformations. Lys_xCBL_y polymers (Fig. 2d) also transitioned toward α-helical or β-sheet structures with rising CBL content, with mixed structures already evident at 40%. This effect likely stems from amide-mediated hydrogen-bonding networks, in line with reports that self-assembling antimicrobial peptides stabilize secondary structures through hydrogen bonding and aromatic interactions.[38]

At 10–40% hydrophobic content, all four series adopted random coil conformations, again attributable to Lys–Lys electrostatic repulsion. Raising the pH, which partially neutralizes cationic groups and mimics anionic bacterial surfaces, induced helix formation in $Lys_{90}CBL_{10}$. This environmental responsiveness demonstrates that conformational adaptability is an intrinsic feature of HDP mimics and may underlie their capacity to tune antibacterial activity.
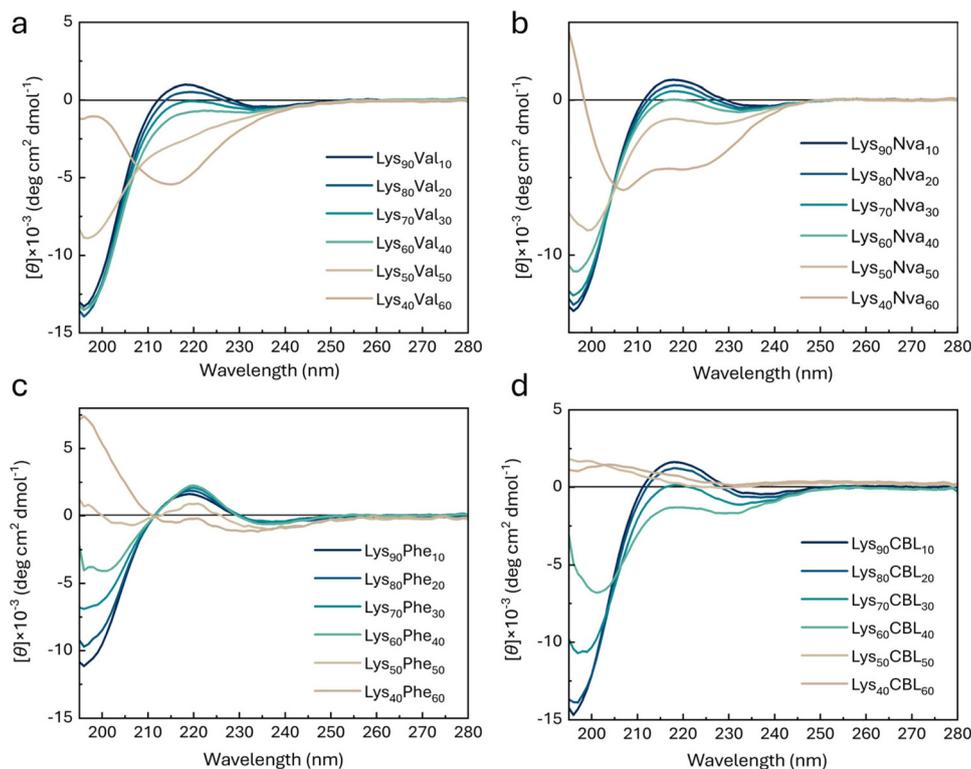
Fig. 2 CD spectra of (a) Lys$_x$Val$_y$, (b) Lys$_x$Nva$_y$, (c) Lys$_x$Phe$_y$ and (d) Lys$_x$CBL$_y$ in PBS buffer (pH 7.4) at 25 °C.

3.4 Structure–function relationships governing the antibacterial activity of HDP mimics against planktonic bacteria

We evaluated the minimum inhibitory concentrations (MICs) and minimum bactericidal concentrations (MBCs) of the polymers against *S. aureus* and *P. aeruginosa* (Table 2). Against *S. aureus*, all four series maintained strong activity at 10–40% hydrophobic content (MIC <12.5 µg mL^{-1}, MBC <25 µg mL^{-1}). Lys$_x$Val$_y$ and Lys$_x$Phe$_y$ were the most potent (MIC = 6.25 µg mL^{-1}), comparable to natural peptides such as lactoferricin B and superior to many reported AMPs.[39–43]

At ≥50% hydrophobicity, trends diverged. Lys$_x$Val$_y$ and Lys$_x$Nva$_y$ showed reduced bactericidal activity, with MBCs rising to 100–200 µg mL^{-1}, likely due to lowered charge density and polymer self-association. In contrast, Lys$_x$Phe$_y$ and Lys$_x$CBL$_y$ retained robust activity, as aromatic stacking or amide hydrogen bonding stabilized interactions when the cationic density decreased.

Against *P. aeruginosa*, Lys$_x$Val$_y$ displayed a bell-shaped activity curve, peaking at intermediate Val levels, whereas Lys$_x$Nva$_y$ maintained low MICs across a broader range (*e.g.*, 3.13 µg mL^{-1} at Lys$_{50}$Nva$_{50}$). Lys$_x$Phe$_y$ and Lys$_x$CBL$_y$ were the most effective at 30–50% hydrophobic content. Notably, large CBL-rich aggregates retained activity comparable to single-chain analogs, indicating that the balance of cationic and hydrophobic groups, rather than the assembly state, governs efficacy.

CD analysis linked these outcomes to the secondary structure. Ordered conformations at high Val or Nva content correlated with diminished bactericidal efficiency, as functional groups became sequestered within folded or aggregated states. This is consistent with previous reports where enforced helicity reduced AMP activity.[40,44,45]

Comparisons across species revealed that Lys$_x$Val$_y$ and Lys$_x$Phe$_y$ were more effective against Gram-positive bacteria, while Lys$_x$Nva$_y$ and Lys$_x$CBL$_y$ favored Gram-negative pathogens. This dichotomy reflects cell envelope differences: Gram-positive bacteria rely primarily on electrostatic interactions with teichoic acids (Fig. S10a), whereas Gram-negative species require additional hydrophobicity to penetrate their lipopolysaccharide-rich outer membrane (Fig. S10b). Despite the random sequence distribution of these copolymers, the overall amphiphilicity proved to be sufficient to reproduce the key functional features of natural HDPs.[46]

In parallel with MICs, NIH/3T3 viability assays show that cytotoxicity varies with the hydrophobic pendant group at equal charge density, consistent with the amphiphilic-balance window observed for antibacterial/antibiofilm activity. This structure dependence motivates prioritizing pendant-group chemistry when modeling and synthesizing next-generation mimics (Fig. S11).[28]

3.5 Non-bactericidal mechanisms and structural determinants underlying biofilm inhibition

In addition to bactericidal activity, HDP mimics inhibited biofilm formation through non-lethal pathways, including interference with bacterial adhesion, quorum sensing, and EPS secretion. Under biofilm-promoting conditions, all four

series suppressed *P. aeruginosa* biofilms in a manner consistent with their antibacterial potency, with Lys_xNva_y showing the strongest inhibition up to 50% Nva before slightly declining (Table 2).

For *S. aureus*, however, inhibition patterns diverged from antibacterial trends. Lys_xVal_y copolymers effectively killed planktonic cells at 10–40% Val but required ~4 × MIC to block biofilm formation, underscoring the tolerance conferred by rapid adhesion and EPS deposition. Notably, $Lys_{50}Val_{50}$, despite weak bactericidal activity (MBC 200 μg mL^{-1}), suppressed >80% of biofilm biomass at 50 μg mL^{-1}, while $Lys_{40}Val_{60}$, though more bactericidal, showed poor antibiofilm performance (Fig. 3a). These discrepancies highlight mechanistic distinctions between cell killing and biofilm inhibition, consistent with natural peptides such as LL-37, which blocks biofilm development at sub-MIC levels through adhesion and signaling interference.[47]

Mechanistic insights suggest that cationic polymers can act at sub-lethal doses by charge neutralization or "bridging effects" that cluster bacteria and reduce surface colonization,[48,49] or by disrupting metabolism and quorum sensing.[50] For example, $Lys_{50}Val_{50}$ assemblies likely adhere to bacterial surfaces, altering hydrophobicity and preventing adhesion.[51]

Lys_xNva_y polymers also displayed strong antibiofilm effects, with $Lys_{50}Nva_{50}$ fully suppressing *S. aureus* biofilms at 50 μg mL^{-1}, below its MBC (Fig. 3b). Similarly, Lys_xPhe_y required higher multiples of MBC at low Phe content but became more efficient at 40–50%, consistent with π–π interactions stabilizing

ordered conformations (Fig. 3c). Lys_xCBL_y showed potent inhibition at 10–40% CBL but diminished efficacy at higher loadings, likely due to the formation of large aggregates that limited cell-surface interactions (Fig. 3d).

Altogether, these results show that antibiofilm activity is not solely dictated by bactericidal potency. Instead, it arises from synergistic contributions of cationic density, moderate hydrophobicity, and specific non-cytotoxic mechanisms, highlighting design opportunities for polymers that target biofilm formation independently of bacterial killing.

3.6 Structural regulation and functional performance in clearing mature biofilms

We next assessed the ability of selected HDP mimics to eradicate established biofilms. Against *S. aureus*, polymers with 10–40% hydrophobic content were the most effective. CLSM imaging with SYTO 9/PI staining revealed that $Lys_{90}Val_{10}$ and $Lys_{80}Val_{20}$ induced extensive bacterial death throughout biofilms, whereas $Lys_{70}Val_{30}$ and $Lys_{60}Val_{40}$ showed residual viability in deeper layers. SEM confirmed pronounced structural damage, including ruptured membranes and collapsed surfaces (Fig. 4a and b). Quantitative assays showed that $Lys_{90}Val_{10}$ cleared 80% of biofilms at 150 μg mL^{-1}, while $Lys_{80}Val_{20}$ required 175 μg mL^{-1}; $Lys_{70}Val_{30}$ removed only ~60% at 200 μg mL^{-1}, and $Lys_{40}Val_{60}$ was largely inactive (Fig. 4c).

In the Lys_xNva_y series, the clearance capacity declined sharply as the cationic content decreased. $Lys_{90}Nva_{10}$ achieved
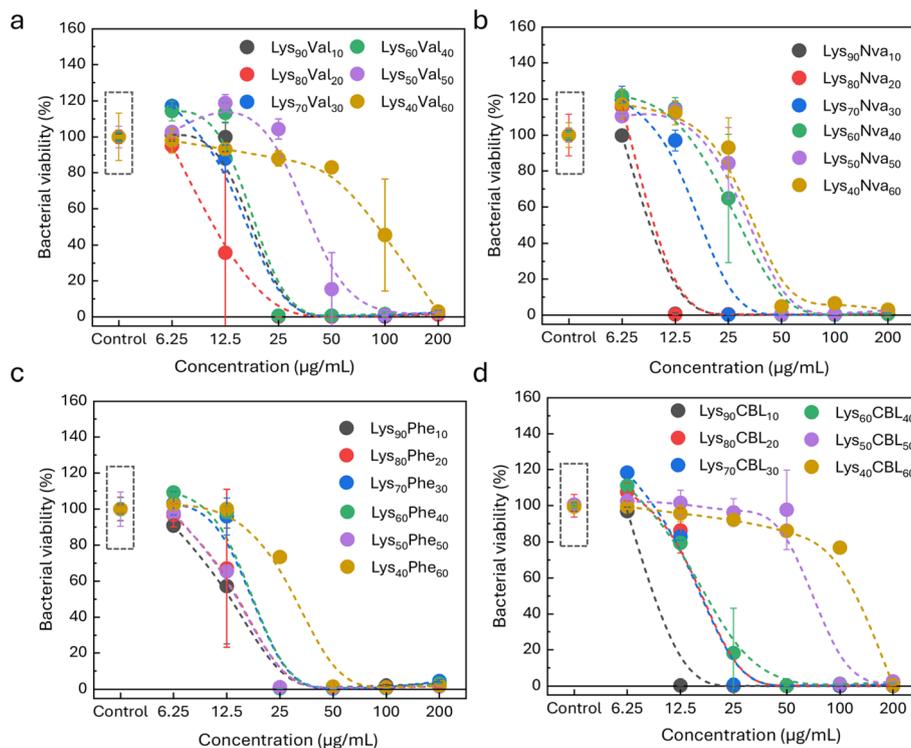

Fig. 3 Quantitative analysis of bacterial viability within biofilms after incubating *S. aureus* in the presence of (a) Lys_xVal_y, (b) Lys_xNva_y, (c) Lys_xPhe_y and (d) Lys_xCBL_y (dashed lines are guides to the eye).
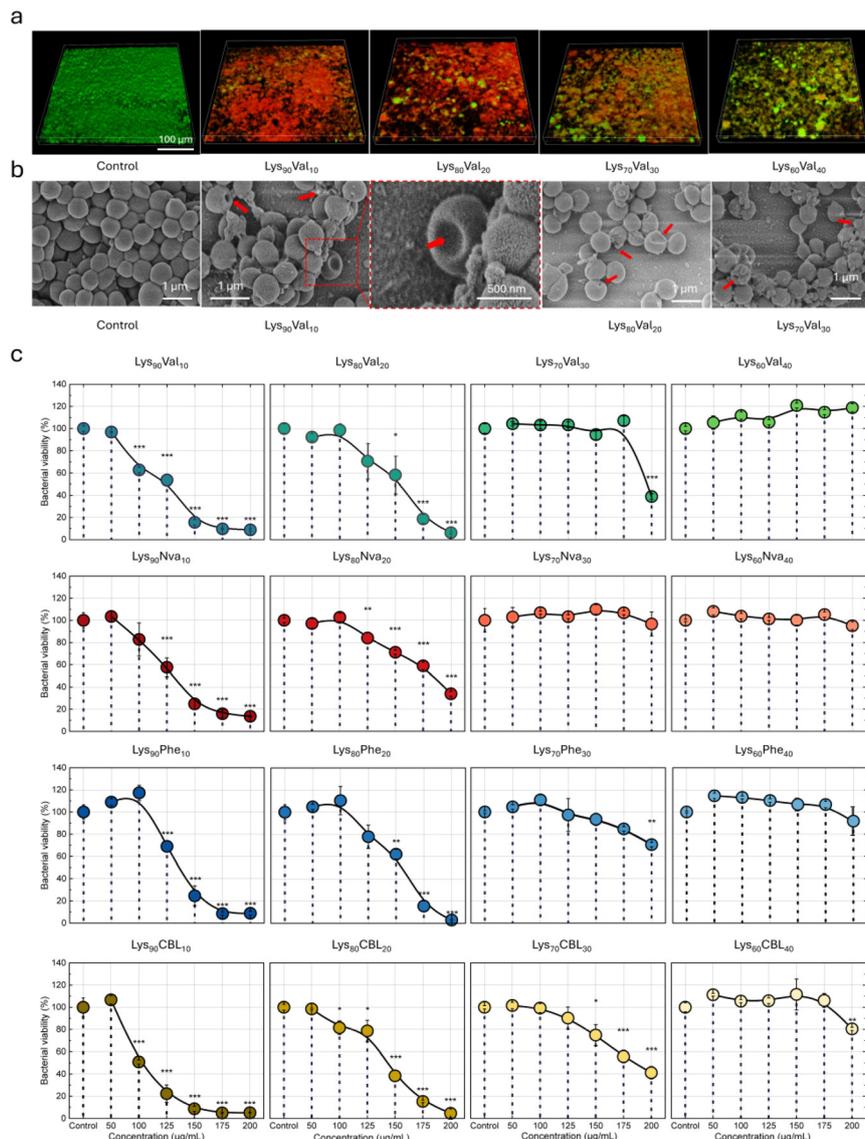
Fig. 4 (a) Three-dimensional confocal laser scanning microscopy (3D CLSM) images of mature *S. aureus* biofilms after 24 h treatment with 200 µg mL^{-1} Lys$_x$Val$_y$. (b) SEM images of biofilms treated with Lys$_x$Val$_y$. (c) Viability of biofilms incubated with Lys$_x$Val$_y$†, Lys$_x$Nva$_y$, Lys$_x$Phe$_y$, or Lys$_x$CBL$_y$ (*$p <$ 0.05, **$p <$ 0.01, *$p <$ 0.001 *vs.* control). † Data adapted from ref. 52, with permission from the Royal Society of Chemistry. Inset: MTT-stained biofilm after polymer treatment.

~80% removal at 150 µg mL^{-1}, but polymers with >20% Nva were ineffective. Lys$_x$Phe$_y$ followed a similar trend: Lys$_{90}$Phe$_{10}$ and Lys$_{80}$Phe$_{20}$ reduced ~80% at 150–175 µg mL^{-1}, whereas higher Phe contents lost efficacy. In contrast, Lys$_x$CBL$_y$ polymers maintained strong performance, with 10–20% CBL clearing >80% of biomass at 125–175 µg mL^{-1}, while Lys$_{70}$CBL$_{30}$ retained ~60% clearance at 200 µg mL^{-1} (Fig. 4c). Collectively, these results underscore that the cationic density dominates EPS penetration and biofilm clearance.

To disentangle charge effects from hydrophobic chemistry, we compared Lys$_{90}$CBL$_{10}$, Lys$_{90}$BA$_{10}$, Lys$_{90}$Leu$_{10}$, and Lys$_{100}$. Despite the identical charge ratios, Lys$_{90}$CBL$_{10}$ achieved near-complete clearance (95%) at 200 µg mL^{-1}, outperforming

Lys$_{90}$BA$_{10}$ (70%) (Fig. 5a). The enhanced activity of CBL arises from amide-mediated hydrogen bonding with EPS and membranes.[16,53] Persister assays confirmed that the amphiphilic balance accelerates clearance: Lys$_{90}$CBL$_{10}$, Lys$_{90}$Val$_{10}$, and Lys$_{90}$BA$_{10}$ eradicated persisters within 18 h, while Lys$_{100}$ required 24 h (Fig. 5b). Consistent with these trends, the biofilm viability decreased in a dose-dependent manner, with Lys$_x$CBL$_y$ and Lys$_x$Val$_y$ showing the steepest reductions, and Lys$_x$Phe$_y$ intermediate and Lys$_x$Nva$_y$ the least (Fig. 5c). Thus, additional cationic charge alone is insufficient; moderate hydrophobicity enhances penetration and killing depth.

For *P. aeruginosa*, polymers with 20–50% hydrophobicity were the most effective. Lys$_x$Nva$_y$ and Lys$_x$CBL$_y$
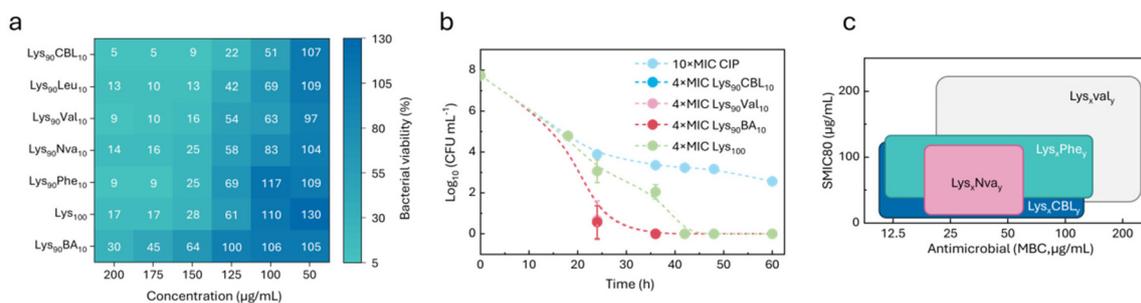
Fig. 5 (a) Eradication efficiency of cationic peptide polymers with different hydrophobic subunits. (b) Killing kinetics of *S. aureus* persister cells treated with polymers at $4 \times$ MIC (induced by CIP at $10 \times$ MIC). (c) Structure–function subset map for *P. aeruginosa*.
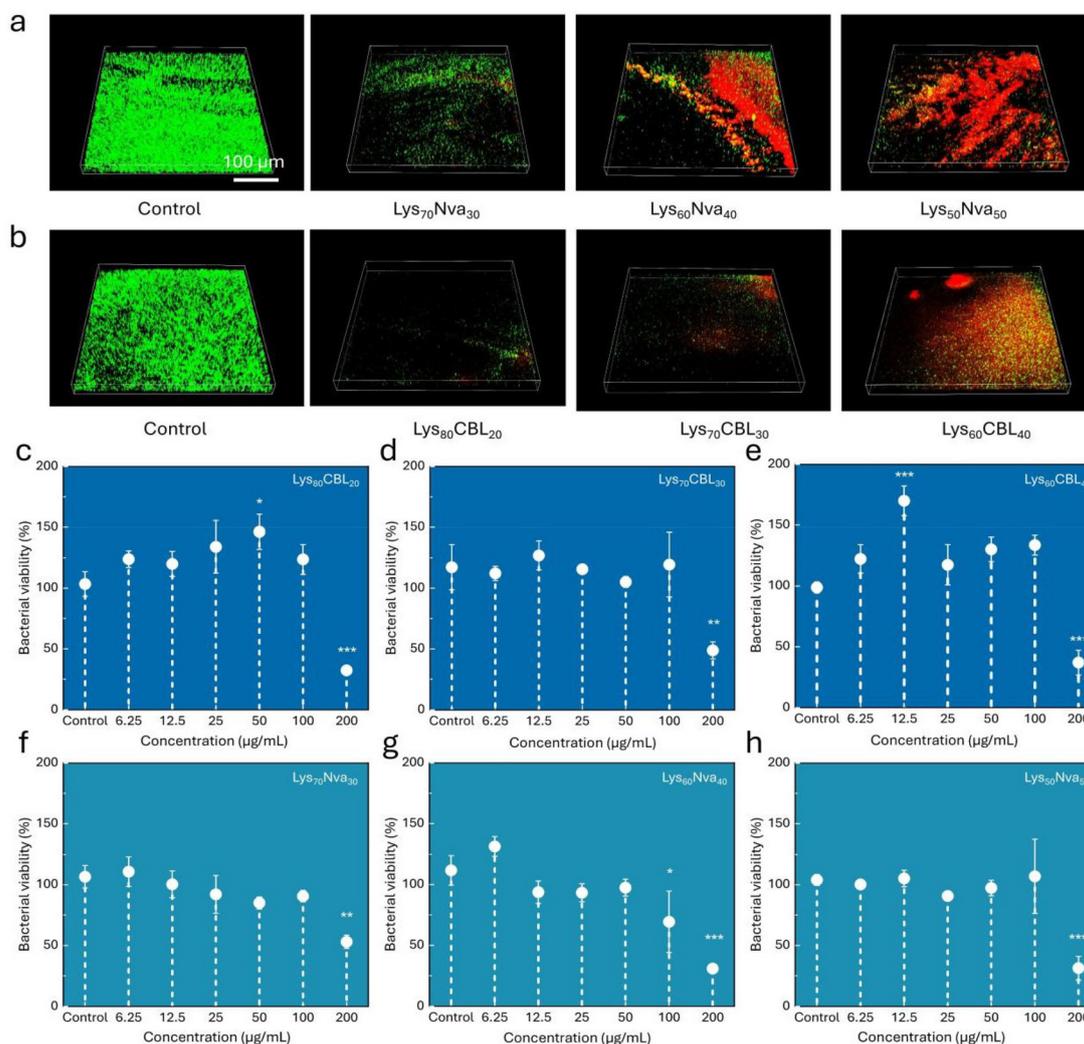

Fig. 6 3D CLSM images of mature *S. aureus* biofilms after 9 h treatment with 200 μg mL^{-1} (a) Lys$_x$Nva$_y$ and (b) Lys$_x$CBL$_y$. Bacterial viability of mature *P. aeruginosa* biofilms after incubation with (c) Lys$_{80}$CBL$_{20}$, (d) Lys$_{70}$CBL$_{30}$, (e) Lys$_{60}$CBL$_{40}$ or (f) Lys$_{70}$Nva$_{30}$, (g) Lys$_{60}$Nva$_{40}$, and (h) Lys$_{50}$Nva$_{50}$ (*$p <$ 0.05, **$p <$ 0.01, and ***$p <$ 0.001; significant difference analysis results were obtained by comparison with the untreated control group).

disrupted the biofilm structure, increased red fluorescence (Fig. 6a and b), and reduced biomass by 50–80% at 200 μg mL^{-1} (Fig. 6c–h).

In contrast, Lys$_x$Val$_y$ and Lys$_x$Phe$_y$ showed limited activity except at specific compositions (Fig. 7a–c). Notably, Lys$_{60}$CBL$_{40}$ was effective against both *S. aureus* and *P. aeruginosa*, likely
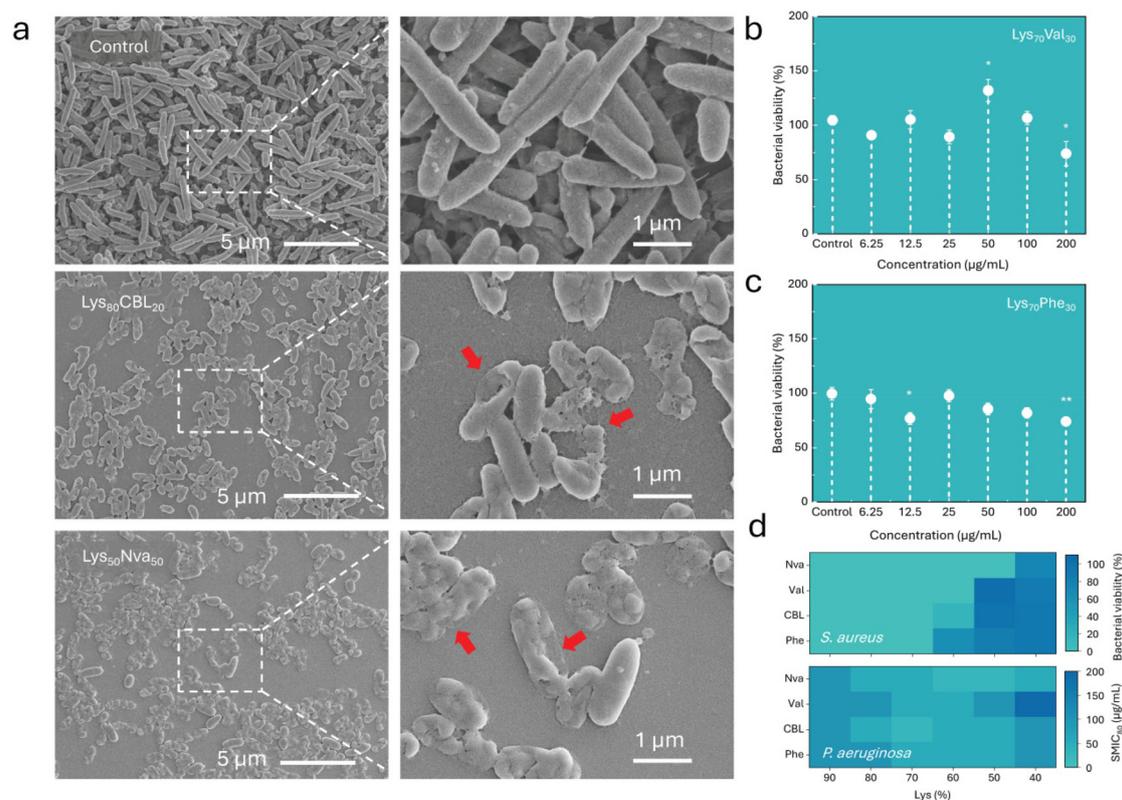
Fig. 7 (a) SEM images of mature *P. aeruginosa* biofilms after treatment with $Lys_{80}CBL_{20}$ or $Lys_{50}Nva_{50}$. Bacterial viability of mature *P. aeruginosa* biofilms after incubation with (b) $Lys_{70}Val_{30}$ or (c) $Lys_{70}Phe_{30}$ (*$p < 0.05$, **$p < 0.01$, and ***$p < 0.001$; significant difference analysis results were obtained by comparison with the untreated control group). (d) Eradication efficiency of cationic peptide polymers with different positive charges and hydrophobic subunits (*S. aureus* biofilm viability was evaluated after exposure to 25 µg mL^{-1} cationic peptide polymers).

due to its higher surface potential (+17.3 mV) compared with $Lys_{50}Nva_{50}$ (+6.9 mV), enabling stronger EPS penetration and adsorption.

Integrating these findings, we constructed a structure–function map (Fig. 7d). High cationic content was decisive for Gram-positive activity, while moderate hydrophobicity enhanced the efficacy against Gram-negative biofilms. Polymers relying solely on charge lacked broad-spectrum antibiofilm potency. Rational amphiphilic designs, balancing charge, hydrophobicity, and assembly properties, therefore represent the optimal strategy for developing HDP mimics capable of eradicating mature biofilms.

3.7 Discussion

With antibiotic resistance intensifying and conventional therapies failing against biofilm-associated infections, this study provides a systematic framework linking the polymer structure to antibacterial and antibiofilm functions. By comparing poly(α-amino acid) copolymers with varied hydrophilic–hydrophobic compositions, we identified how the cationic density, hydrophobicity, and assembly behaviour cooperatively shape biological outcomes.

Our results demonstrate that the cationic charge density is the primary driver of EPS penetration and biofilm clearance. Polymers with high Lys content, such as $Lys_{90}Val_{10}$ and

$Lys_{90}CBL_{10}$, readily permeated and disrupted mature *S. aureus* biofilms, while reducing charge below ~60% led to a sharp loss of efficacy. This underscores the central role of electrostatics in overcoming the biofilm barrier.

Hydrophobicity further modulated activity, especially against *P. aeruginosa*. Polymers incorporating Nva or CBL performed best at intermediate hydrophobic ratios (20–40%), where solubility, membrane affinity, and EPS interactions were optimally balanced. CBL's amide side chains provided additional hydrogen bonding, conferring advantages over Val, Phe, or ester-containing BA.

Self-assembly also proved critical. $Lys_{60}CBL_{40}$ formed nanoscale aggregates with higher surface potential (+17.3 mV), enabling deep EPS penetration and persister eradication, whereas $Lys_{50}Nva_{50}$, despite similar composition, lacked comparable activity due to its lower charge density and weaker assemblies. Persister assays confirmed that amphiphilicity, not charge density alone, governs clearance kinetics: $Lys_{90}CBL_{10}$, $Lys_{90}Val_{10}$, and $Lys_{90}BA_{10}$ eradicated persisters faster than fully cationic Lys_{100}.

Importantly, antibacterial potency against planktonic bacteria and antibiofilm efficacy were not linearly correlated. While electrostatic adsorption dominates activity against Gram-positive bacteria, moderate hydrophobicity is essential
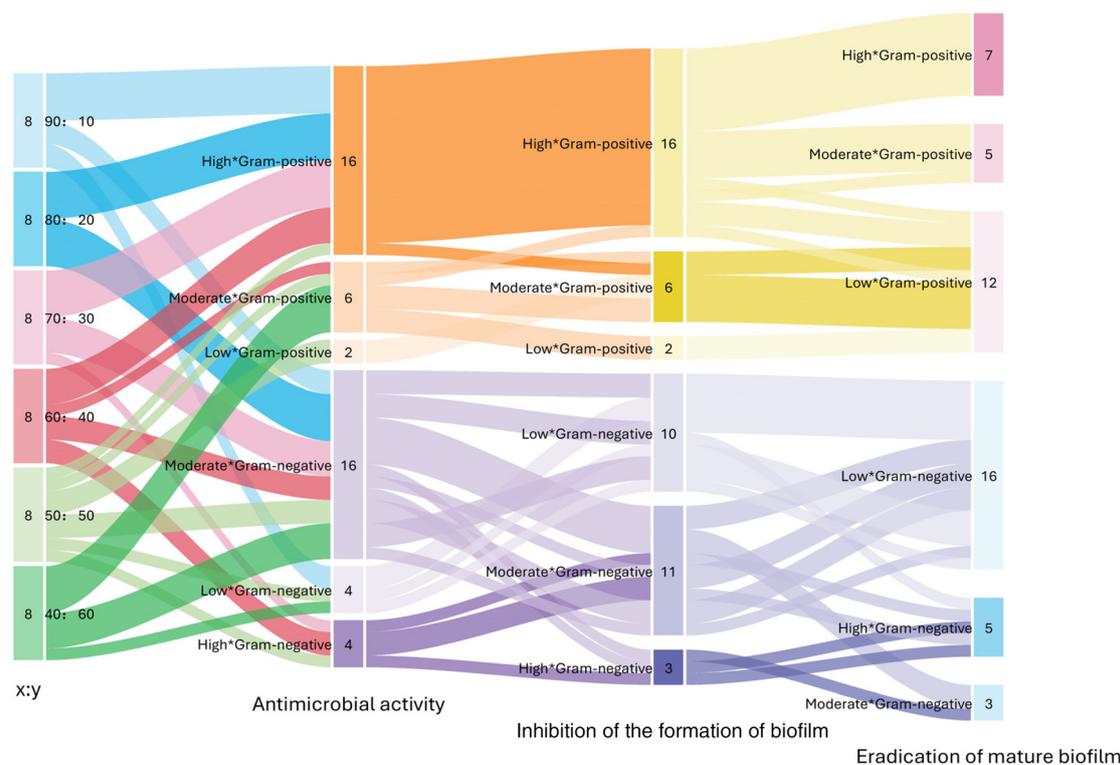
Fig. 8 Sankey diagram correlating the cationic peptide polymer composition with their ability to eradicate *S. aureus* or *P. aeruginosa* biofilm. Lys_xY_y = x mol% Lys and y mol% hydrophobic unit ($x + y = 100$; Y = Val/Nva/Phe/CBL).

for breaching Gram-negative outer membranes and their biofilms. This distinction highlights that separate mechanisms underlie these two activities, requiring differentiated design strategies.

In addition to improvements in process greenness,[54] the comparative sustainability of peptide-based antimicrobials relative to conventional antibiotics merits attention. Antibiotic production and environmental fate analyses have shown that active pharmaceutical ingredient synthesis accounts for nearly 40–45% of the total life-cycle environmental impact,[55] and persistent residues contribute to antimicrobial resistance dissemination. In contrast, antimicrobial peptides and their mimics are enzymatically degradable and exhibit effective antibiofilm activity at 10–100 μg mL^{-1}.[56,57] When compared on a functional unit basis (≥90% mature biofilm clearance), the lower mass and energy demands per antibacterial effect indicate that HDP-based systems inherently align with green chemistry principles by reducing the persistence, resistance potential, and material intensity.[32]

Overall, our study clarifies the cooperative roles of cationic density, moderate hydrophobicity, and self-assembly in defining the dual functionality of HDP mimics (Fig. 8). These insights provide design principles for amphiphilic polymers capable of both killing planktonic bacteria and clearing mature biofilms, offering a rational path toward next-generation biomimetic therapeutics for multidrug-resistant and chronic biofilm-associated infections.

4. Conclusion

This study elucidates composition–structure–function relationships in cationic copolypeptides for biofilm eradication and demonstrates that the underlying synthetic route achieves high efficiency with reduced material and energy demands. The moisture-tolerant, catalyst-free NCA process yields 74% conversion—an improvement over conventional peptide-synthesis routes—while lowering the E-factor and PMI by about 50% and halving the energy requirement. These quantitative reductions provide clear evidence of an environmentally improved process consistent with the current principles of green chemistry.

Beyond process optimization, host defense peptide mimics represent an environmentally responsible antimicrobial platform. Compared with small-molecule antibiotics—which often show persistence in water environments and contribute to antimicrobial resistance—biodegradable peptides offer comparable efficacy with lower functional-unit mass and minimal long-term environmental footprint. This work therefore underscores how the rational design and sustainable synthesis of HDP-based materials can jointly advance the dual objectives of biomedical performance and green chemistry sustainability.

Conflicts of interest

The authors declare no conflict of interest.

Data availability

The data supporting the findings of this study are available within the article and its supplementary information (SI). Supplementary information is available. See DOI: https://doi.org/10.1039/d5gc05877e.

Acknowledgements

References

1 J. W. Costerton, P. S. Stewart and E. P. Greenberg, *Science*, 1999, **284**, 1318–1322.
2 H.-C. Flemming and J. Wingender, *Nat. Rev. Microbiol.*, 2010, **8**, 623–633.
3 C. R. Arciola, D. Campoccia and L. Montanaro, *Nat. Rev. Microbiol.*, 2018, **16**, 397–409.
4 W. Zhang, S. Deng, M. Zhou, J. Zou, J. Xie, X. Xiao, L. Yuan, Z. Ji, S. Chen, R. Cui, Z. Luo, G. Xia and R. Liu, *Biomater. Sci.*, 2022, **10**, 4515–4524.
5 Z. Si, W. Zheng, D. Prananty, J. Li, C. H. Koh, E.-T. Kang, K. Pethe and M. B. Chan-Park, *Chem. Sci.*, 2022, **13**, 345–364.
6 R. A. Sheldon, *Green Chem.*, 2017, **19**, 18–43.
7 J. Li, E. M. Simmons and M. D. Eastgate, *Green Chem.*, 2017, **19**, 127–139.
8 E. Lucas, A. J. Martín, S. Mitchell, A. Nabera, L. F. Santos, J. Pérez-Ramírez and G. Guillén-Gosálbez, *Green Chem.*, 2024, **26**, 9300–9309.
9 M. Di Consiglio, E. Sturabotti, B. Brugnoli, A. Piozzi, L. M. Migneco and I. Francolini, *Polym. Chem.*, 2023, **14**, 432–442.
10 D. G. J. Larsson and C.-F. Flach, *Nat. Rev. Microbiol.*, 2022, **20**, 257–269.
11 C. A. Davis and E. M.-L. Janssen, *Environ. Int.*, 2020, **134**, 105271.
12 P. Ma, Y. Wu, W. Jiang, N. Shao, M. Zhou, Y. Chen, J. Xie, Z. Qiao and R. Liu, *Biomater. Sci.*, 2022, **10**, 4193–4207.
13 Y.-M. Wu, K. Chen, J. Wang, W. Dai, H. Yu, X. Xie, M. Chen and R.-H. Liu, *Nat. Protoc.*, 2025, **20**, 709–726.
14 Z.-Y. Tian, Z. Zhang, S. Wang and H. Lu, *Nat. Commun.*, 2021, **12**, 5810.
15 D. Reinhardt, F. Ilgen, D. Kralisch, B. König and G. Kreisel, *Green Chem.*, 2008, **10**, 1170–1181.
16 H. C. Erythropel, *et al.*, *Green Chem.*, 2018, **20**, 1929–1961.
17 F. Roschangar, R. A. Sheldon and C. H. Senanayake, *Green Chem.*, 2017, **19**, 281–285.
18 J. L. Osorio-Tejada, F. Ferlin, L. Vaccaro and V. Hessel, *Green Chem.*, 2023, **25**, 9760–9778.
19 T. Yamaki, *et al.*, *Green Chem.*, 2024, **26**, 3758–3766.
20 A. Bardow, J. Pérez-Ramírez, S. Sala and L. Vaccaro, *Green Chem.*, 2024, **26**, 11016–11018.
21 V. G. Zuin, I. Eilks, M. Elschami and K. Kümmerer, *Green Chem.*, 2021, **23**, 1594–1608.
22 P. M. Nowak, *Green Chem.*, 2023, **25**, 4625–4640.
23 C. Jiménez-González, C. S. Ponder, Q. B. Broxterman and J. B. Manley, *Org. Process Res. Dev.*, 2011, **15**, 912–917.
24 D. Zhang, Y. Qian, S. Zhang, P. Ma, Q. Zhang, N. Shao, F. Qi, J. Xie, C. Dai, R. Zhou, Z. Qiao, W. Zhang, S. Chen and R. Liu, *Sci. China Mater.*, 2019, **62**, 604–610.
25 H. R. Kricheldorf, *Angew. Chem., Int. Ed.*, 2006, **45**, 5752–5784.
26 C. A. Stewart and C. A. VanderWerf, *J. Am. Chem. Soc.*, 1954, **76**, 1259–1264.
27 E. F. Palermo, D.-K. Lee, A. Ramamoorthy and K. Kuroda, *J. Phys. Chem. B*, 2011, **115**, 366–375.
28 D. S. S. M. Uppu, M. M. Konai, U. Baul, P. Singh, T. K. Siersma, S. Samaddar, S. Vemparala, L. W. Hamoen, C. Narayana and J. Haldar, *Chem. Sci.*, 2016, **7**, 4613–4623.
29 G. N. Tew, R. W. Scott, M. L. Klein and W. F. DeGrado, *Acc. Chem. Res.*, 2010, **43**, 30–39.
30 H. Etayash and R. E. W. Hancock, *Pharmaceutics*, 2021, **13**, 1820.
31 G. J. M. Habraken, K. H. R. M. Wilsens, C. E. Koning and A. Heise, *Polym. Chem.*, 2011, **2**, 1322–1330.
32 H.-K. Lin, C.-H. Dai, T. F. Jamison and K. F. Jensen, *Angew. Chem., Int. Ed.*, 2017, **56**, 8870–8873.
33 V. Tulus, J. Pérez-Ramírez and G. Guillén-Gosálbez, *Green Chem.*, 2021, **23**, 9881–9893.
34 T. Yang, T. Xue, J. Mao, Y. Chen, H. Tian, A. Bartolome, H. Xia, X. Yao, C. V. Kumar, J. Cheng and Y. Lin, *J. Am. Chem. Soc.*, 2024, **146**, 5823–5833.
35 N. J.-A. Chan, D. Gu, S. Tan, Q. Fu, T. G. Pattison, A. J. O'Connor and G. G. Qiao, *Nat. Commun.*, 2020, **11**, 1630.
36 S. Yamashita and T. Yamashita, *Proc. Natl. Acad. Sci. U. S. A.*, 1975, **72**, 941–942.
37 S. Y. Lau, A. K. Taneja and R. S. Hodges, *J. Biol. Chem.*, 1984, **259**, 13253–13261.
38 H. Liu, Z. Song, Y. Zhang, B. Wu, D. Chen, Z. Zhou, H. Zhang, S. Li, X. Feng, J. Huang and H. Wang, *Nat. Mater.*, 2025, **24**, 1295–1306.
39 J. Turner, Y. Cho, N.-N. Dinh, A. J. Waring and R. I. Lehrer, *Antimicrob. Agents Chemother.*, 1998, **42**, 2206–2214.
40 J. Harder, J. Bartels, E. Christophers and J.-M. Schröder, *J. Biol. Chem.*, 2001, **276**, 5707–5713.
41 H. Raghuraman and A. Chattopadhyay, *Biosci. Rep.*, 2007, **27**, 189–223.
42 Ø. Samuelsen, H. H. Haukland, H. Jenssen, M. Krämer, K. Sandvik, H. Ulvatne and L. H. Vorland, *FEBS Lett.*, 2005, **579**, 3421–3426.
43 Y. Ge, D. L. MacDonald, K. J. Holroyd, C. Thornsberry, H. Wexler and M. Zasloff, *Antimicrob. Agents Chemother.*, 1999, **43**, 782–788.
44 T. L. Raguse, E. A. Porter, B. Weisblum and S. H. Gellman, *J. Am. Chem. Soc.*, 2002, **124**, 12774–12785.

45 A. M. Carmona-Ribeiro and L. D. de Melo Carrasco, *Int. J. Mol. Sci.*, 2013, **14**, 9906–9946.

46 M. A. Gelman, B. Weisblum, D. M. Lynn and S. H. Gellman, *Org. Lett.*, 2004, **6**, 557–560.

47 J. Overhage, A. Campisano, M. Bains, E. C. W. Torfs, B. H. A. Rehm and R. E. W. Hancock, *Infect. Immun.*, 2008, **76**, 4176–4182.

48 L. L. Foster, S.-i. Yusa and K. Kuroda, *Antibiotics*, 2019, **8**, 61.

49 L. R. Martinez, M. R. Mihu, G. Han, S. Frases, R. J. B. Cordero, A. Casadevall, A. J. Friedman, J. M. Friedman and J. D. Nosanchuk, *Biomaterials*, 2010, **31**, 669–679.

50 H. Lu, C. Tu, T. Zhou, W. Zhang, Y. Zhan, J. Ding, X. Wu, Z. Yang, W. Cao, L. Deng, C. Gao and F. Xu, *Chem. Eng. J.*, 2022, **436**, 135130.

51 Y. Yang, Y. Qian, M. Zhang, S. Hao, H. Wang, Y. Fan, R. Liu, D. Xu and F. Wang, *J. Mater. Sci. Technol.*, 2023, **133**, 77–88.

52 Y. Bi, X. Chen, F. Luo, X. Wang, X. Chen, J. Yao and Z. Shao, *Biomater. Sci.*, 2024, **12**, 5337–5348.

53 D. S. S. M. Uppu, S. Samaddar, J. Hoque, M. M. Konai, P. Krishnamoorthy, B. R. Shome and J. Haldar, *Biomacromolecules*, 2016, **17**, 3094–3102.

54 O. Al Musaimi, B. G. de la Torre and F. Albericio, *Green Chem.*, 2020, **22**, 996–1018.

55 K. Yang, B. Lv, H. Shen, G. Jing and Z. Zhou, *Int. J. Life Cycle Assess.*, 2021, **26**, 64–75.

56 G. Batoni, G. Maisetta and S. Esin, *Biochim. Biophys. Acta*, 2016, **1858**, 1044–1060.

57 E. Galdiero, L. Lombardi, A. Falanga, G. Libralato, M. Guida and R. Carotenuto, *Pharmaceutics*, 2019, **11**, 322.